Theoretical Application of Short-Lag Spatial Coherence to Photoacoustic Imaging

Michelle T. Graham[1] and Muyinatu A. Lediju Bell[1,2]

[1]Department of Electrical and Computer Engineering, *Johns Hopkins University, Baltimore, MD*
[2]Department of Biomedical Engineering, *Johns Hopkins University, Baltimore, MD*

***Abstract*—Short-Lag Spatial Coherence (SLSC) is a beamforming technique that was initially developed for ultrasound imaging, then applied to photoacoustic imaging with considerable improvements in contrast and signal-to-noise ratios, when compared to traditional delay-and-sum beamforming. However, these applications suffer from the lack of a well validated theory to support its implementation. We are developing spatial coherence theory for SLSC beamforming of photoacoustic images to better understand the breadth of potential applications and their associated limitations. The objective of this work is to further explore this theory and validate it, primarily with experimental data. A spatial coherence equation was derived based on the van Cittert-Zernike theorem and a linear system that describes the photoacoustic imaging process. This equation was evaluated to generate spatial covariance curves and SLSC lateral profiles for targets of diameters 1.3 to 10 mm. Theoretical profiles were compared to experimental data. The theoretical photoacoustic spatial covariance curves exhibited strong similarity to experimental data, although we observe differences outside of the short-lag region and in the noise floor of SLSC profiles. We show that we can model different absorber sizes and that the incident laser profile influences the spatial coherence curve, resulting SLSC profiles, and the associated SLSC image contrast.**

***Index Terms*—photoacoustic, short-lag spatial coherence, van-Cittert Zernike**

I. Introduction

Short-lag spatial coherence (SLSC) is a beamforming technique that was initially developed for ultrasound imaging, demonstrating considerable improvements in contrast, contrast-to-noise ratio, and signal-to-noise ratio, compared to traditional delay-and-sum (DAS) beamforming. Novel in its approach of using coherence values directly for image formation, as opposed to amplitude measurements, SLSC performs particularly well in high noise environments [1].

Mallart and Fink developed a theoretical formalism of spatial coherence for pulse-echo ultrasound using the fundamental van Cittert-Zernike theorem of optics, which describes the autocorrelation of a wave field produced by an incoherent source [2]. This description was then used to derive the theory for SLSC beamforming of ultrasound data and to implement it experimentally [1].

The SLSC technique was later applied to experimental photoacoustic imaging (PAI) with similar improvements. In PAI the thermal expansion and contraction of light absorbing targets emits an acoustic wave, recieved by an ultrasound transdcuer. PAI is advantageous in its sensitivity to chromophores, such as hemoglobin, by altering the exciting wavelength based on the target's optical absorption spectrum [3]. Because it is independent of signal amplitude, SLSC is particularly beneficial for photacoustic imaging in scenarios of low laser fluence incident on the target, such as when imaging deep structures like brachytherapy seeds [4] or when using low-cost, low-energy, easily transportable pulsed laser diodes [5]. However, a theory describing this performance was never derived.

The purpose of this work is to use the VCZ theorem to develop a photoacoustic-specifc spatial coherence theory to enable optimization of coherence-based photoacoustic images. We start by deriving a theoretical equation of photoacoustic spatial covariance, which is subsequently used to formulate an equation of photoacoustic SLSC beamforming. We then compare our theoretical simulations to experimental data from cylindrical targets for validation.

II. Photoacoustic Spatial Coherence

Similar to ultrasound imaging, where the measured pressure field received by the transducer can be described by a linear system of three terms (transmit ultrasound beam, random distribution of scatterers, and propagation of the sound wave back to the transducer), a three term linear systems approach is used to describe the measured photoacoustic pressure field, P. The photoacoustic-specific terms are:

1) L, the initial pressure distribution at the absorber surface at a position X_o, dependent on tissue properties (Gruneisen parameter, Γ, optical absorption coefficient, μ_a) and on the fluence at depth z: $F(z, \mu_a) = F_o e^{-\mu_a z}$.
2) χ, the random distribution of spatially incoherent absorbers (also known as the source function or source distribution function) at source location X_0.
3) H_{rx}, the spherical propagation of the sound wave from the source to a point, n, on the transducer:

$$H_{rx}(X_0, X_n, f) = \frac{e^{j2\pi f r/c}}{r_{0n}} \tag{1}$$

with speed of sound, c, travel distance, r, and a acoustic frequency, f, related to the bandwidth of the ultrasound transducer.

The acoustic pressure measured along a transducer is therefore defined in the spatial frequency domain as:

$$P(X_0, X_n, f) = L(X_0, f)\chi(X_0, f)H_{rx}(X_0, X_1, f) \tag{2}$$

where X_n is a point on the aperture.

The total received pressure at a point on the aperture, X_1, is found by integrating the pressure field over the isochronous volume of interest.

$$P(X_1, f) = \iiint_V P(X_0, X_1, f)\, d^3X_0 \tag{3}$$

Note that Eq. (3) is similar to Eq. (2) in Ref. [6].

The axial dimension (z) is assumed to be constant, reducing the volume integral in Eq. (3) to a surface integral. Because the lateral and elevation dimensions are separable, the surface integral is reduced to a linear integral in the lateral dimension.

The spatial covariance, R, is the correlation of the pressure field at two lateral receiving positions X_1 and X_2:

$$R_p(X_1, X_2, f) = \langle P(X_1, f), P^*(X_2, f) \rangle \tag{4}$$

We then utilize the properties of random spatially incoherent distributions, which describes the source function $\chi(f)$, sifting property of the delta function, and the Fresnel approximation to yield an equation for photoacoustic spatial covariance.

$$R_p(x_1, x_2, x, z, \lambda) = \frac{e^{(j\pi(x_1 x_1 - x_2 x_2)/\lambda z}}{z^2} \cdot \int_{-\infty}^{\infty} \mid \chi_o(f)\Gamma(x)\mu_a F_o(x) e^{-\mu_a z} \mid^2 e^{-j2\pi(x(x_1 - x_2))/\lambda z} dx \tag{5}$$

Eq. (5) is the scaled Fourier transform of the square of χ_o multiplied by L, and this Fourier transform is multiplied by a phase term.

We first make the assumption that the transducer is symmetric about its center, which initially eliminates the phase term. With this symmetry assumption, we can only image the axial line corresponding to the lateral position of the center of the aperture. To obtain the full region of interest to the left and right of the center, we divide our aperture into sub-apertures. Each sub-aperture obeys the symmetry assumption and is symmetric about its center. We shift the center of the sub-aperture by a distance x_k to obtain each successive lateral line of interest until we visualize the entire physical imaging region. This process, depicted in Fig. 1, is mathematically defined as the shifting property of the Fourier transform where a shift in space corresponds to a multiplication by a phase term in the spatial frequency domain. This yields our final photoacoustic spatial covariance equation, with a new phase term.

$$R_p(\mathfrak{m}, x - x_k, z, \lambda) = e^{-(j2\pi x_k \mathfrak{m})/\lambda z} \cdot \int_{-\infty}^{\infty} z^{-2} \mid \chi(f)\Gamma(x)\mu_a F_o(x) e^{-\mu_a z} \mid^2 e^{-(j2\pi x \mathfrak{m})/\lambda z} dx \tag{6}$$

where lag is given by $\mathfrak{m} = x_1 - x_2$. The phase term in Eq. (6) is equivalent to the phase term in Eq. (5), but Eq. (6) is more generalizable because the x_k and $\mathfrak{m}$ terms remove the direct dependence on specific lateral positions x_1 and x_2.

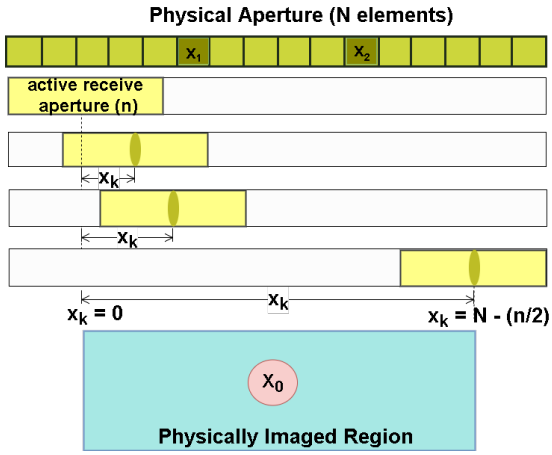

Fig. 1: The symmetry assumption is satisfied by partitioning the physical aperture of N elements into active receiving sub-apertures of n elements. The active apertures are symmetric about their centers (oval) and shifted by distances x_k, from $x_k = 0$ to $x_k = N - (n/2)$, to image the entire region of interest.

Eq. (6) is used to find a purely coherence based pixel value in photoacoustic SLSC beamforming.

$$SLSC_{pixel}(x_k, z) = \int_0^M R_p(m, x - x_k, z, \lambda) dm \tag{7}$$

where the shift, x_k, indicates the lateral position of the axial line of interest, and M is the chosen short-lag value. Therefore, to obtain a theoretical SLSC image, a coherence curve must be generated using Eq. (6) and subsequently integrated using Eq. (7), for each pixel.

III. Methods

A. Theoretical Simulations

A virtual 2D phantom was designed in MATLAB, its lateral dimension corresponding to the lateral dimension of an ultrasound transducer and axial dimension corresponding to the depth of the imaging plane. A virtual ultrasound transducer, modeled after the Alpinion L3-8 transducer, was placed at depth = 0 m. Circular targets of high optical absorption were placed in a background of low optical absorption, within the high fluence area of the Gaussian laser beam profile (Fig. 2). These targets measured 1.3 mm to 10 mm in diameter. The beam fluence profile was modeled after that of the 1 mm core optical fiber. The $1/e$ width of the Gaussian beam was limited to 1.3 mm, which is smaller than most of the target sizes, as illustrated in Fig. 2. We also explored illuminating the entire field with a wider light sheet (not shown) and compared resulting SLSC profiles.

B. Experimental Data

Tubing of inner diameters 1.3 mm - 10 mm were submerged in a water bath and used as photoacoustic targets. This tubing was rigidly fixed in an acrylic apparatus and first filled with water as a control, to obtain the photoacoustic signal of the tubing alone. The water was aspirated out and subsequently replaced with a 0.067 % India Ink solution without altering

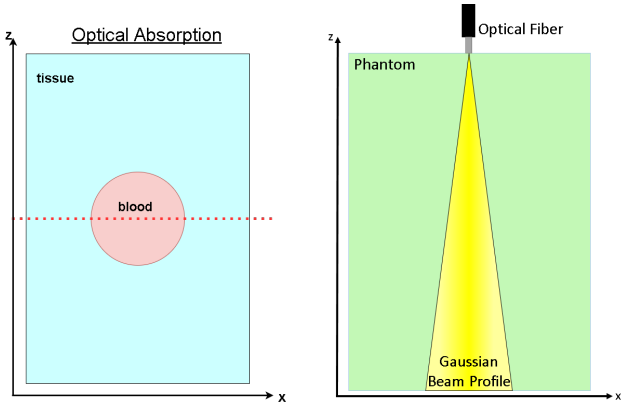

(a) (b)

Fig. 2: (a) 2D optical absorption distribution simulating a blood vessel of high optical absorption in diffuse tissue of low optical absorption. (b) 2D Fluence distribution modeling a Gaussian beam profile from an optical fiber.

the tubing position, enabling discrimination of signals from the tubing walls relative to signals from the India Ink. A 1 mm core diameter optical fiber (multimode, 0.5 NA) was coupled to the 1064 nm output port of an Opotek Phocus Mobile system (Carlsbad, CA) operating with 1.5 mJ per pulse. Photoacoustic channel data was collected with an Alpinon (Bothell, WA) E-Cube 12R scanner connected to an Alpinion L3-8 linear transducer probe. The transducer was positioned such that the circular cross section of the tubing diameter was in the imaging plane.

IV. Results and Discussion

A. Tubing Targets

Fig. 3(a) shows an experimental SLSC ($M = 10$) image of a 10 mm diameter tubing cross section. The SLSC pixel values at a depth of 2.4 mm (corresponding to the center of the target in the depth dimension) were displayed as a function of their lateral positions to create a SLSC line plot for comparison with theoretical results (Fig. 3(b)). The theory accurately localized and visualized the target.

To obtain the theoretical SLSC line plots, the Fourier transform was first evaluated at appropriate spatial frequencies of the photoacoustic signal profile, resulting in one spatial covariance curve for each lateral position. Integrating the spatial covariance up to a chosen lag (Eq. (7)) provided the coherence value for image display.

For the 10 mm target, theoretical and experimental spatial covariance curves exhibit strong similarity in the short-lag region both in the area of high photoacoustic absorption inside the target (Fig. 3(c)) and in the area of low photoacoustic absorption outside the target (Fig. 3(d)). Inside the target (Fig. 3(c)), at the lateral position marked by the gray vertical line in Fig. 3(b), the theoretical and experimental spatial covariance curves follow a Gaussian distribution in the short-lag region (the region of interest in SLSC imaging). Integration of these curves provides high SLSC values. These experimental curves also exhibit sinc-like properties at higher lags, which are not present in the theory. As M is typically constrained to 30% of the aperture [1], the dissimilarities in the high lag region do not impact the SLSC line plots. Outside the target, the spatial covariance curves are dominated by incoherent noise (Fig. 3(d)). Their integration provides a low SLSC value, giving the floor of the SLSC line plots (Fig. 3(b)). Despite the oscillations observed in the floor of the SLSC line plots, there is generally good agreement of theoretical and experiment results for the 10 mm diameter target.

Fig. 4 demonstrates the effect of the fluence profile on the line plots for 1.3, 4, and 10 mm target sizes. The theory successfully models different target sizes when the beam profile is implemented as a light sheet that illuminates the entire target (Fig. 4(a)).

When the fluence profile is physically constrained to a narrow Gaussian distribution (to model the optical fiber used in experiments), the imaged targets are smaller than the true tubing diameter for the larger 4 mm and 10 mm targets (Fig. 4(b)). The theoretical targets appear similar in size, which is also observed experimentally (Fig. 4(c)) for the same size targets.

Fig. 4 additionally shows that contrast increases with decreasing target size for both theoretical and experimental data. The broad spatial domain photoacoustic signals for large targets equate to a narrow mainlobe in the spatial

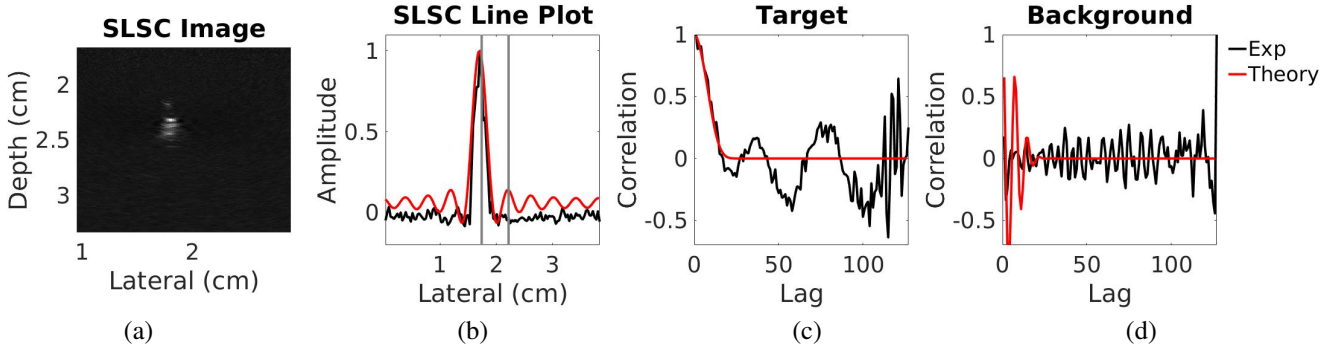

(a) (b) (c) (d)

Fig. 3: Comparison of theoretical and experimental data from a 10 mm diameter target. (a) The SLSC ($M = 10$) experimental image is isolated at the depth of the target center. (b) The SLSC line plot is displayed for that depth. (c) The spatial covariance curves of the target region and (d) background region are shown at locations corresponding to the lateral location of the gray marker lines on the SLSC line plot.

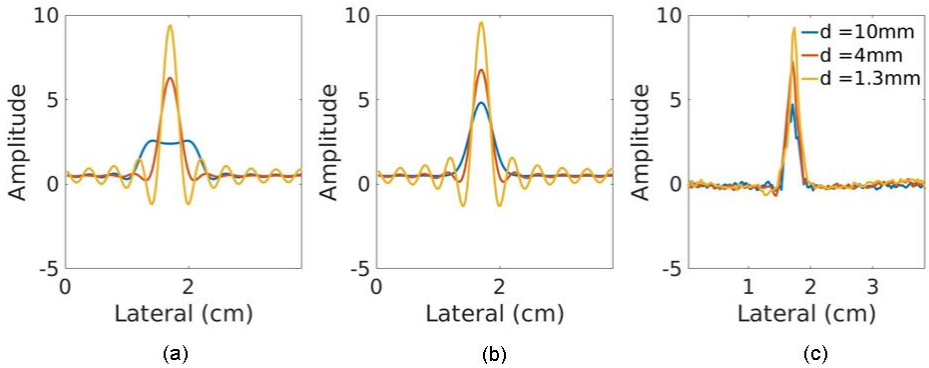

Fig. 4: SLSC line plots of 10 mm, 4 mm, and 1.3 mm diameter targets are displayed for theoretical data obtained with (a) light sheet and (b) Gaussian beam illumination and the corresponding line plots for (c) experimental data. All line plots were created with $M = 10$.

frequency domain of the coherence curves. With less area under the curve, larger targets have a lower integrated SLSC amplitude value. This effect on amplitude is observed for the theoretical results with both laser beam profiles (light sheet and Gaussian). It is additionally interesting to note that we obtain greater contrast for the 10 mm target when the 1.3 mm Gaussian beam is used instead of the light sheet. These results indicate that the narrow Gaussian beam dominates to determine the shape and width of the photoacoustic signal profile when the target is larger than the beam, and contrast is increased because the entire target size partially contributes to the spatial coherence curve. This partial contribution likely occurs because the optical absorption of the portion of the target external to the Gaussian beam is high enough to absorb some of the light external to the 1/e diameter of the beam. For the theoretical results, this external profile is included before applying the Fourier transform described in Eq. (6).

B. Effect of the Short-Lag Value

Fig. 5 demonstrates the effect of varying the lag, M, for SLSC line plot display of a 10 mm diameter target. For both theoretical (Fig. 5(a)) and experimental data (Fig. 5(b)), the target's full-width-at-half-maximum (FWHM) decreases as M increases within the short-lag region. Theoretical simulations have a wider FWHM at low lags ($M < 5$) than experimental data for the same target size. These results give initial insight that photoacoustic SLSC lateral resolution improves with increasing M, a trend that was previously demonstrated experimentally [1]. Our theory enables us to choose the minimum M that will optimize image resolution.

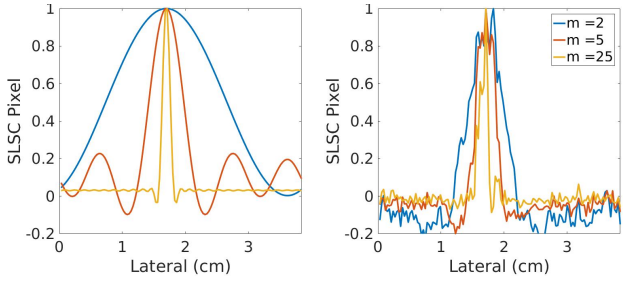

Fig. 5: SLSC line plots of a 10 mm diameter target are displayed for (a) theoretical and (b) experimental data at lags M = 2, 5, and 25.

V. Conclusion

This work is the first to derive a theoretical expression for photoacoustic spatial covariance, and utilize it to model theoretical short-lag spatial coherence data. The theory generally agrees with experimental data for high absorbing circular targets of diameters 1.3 mm to 10 mm when visualizing both spatial covariance curves and SLSC line plots. Although the target size varies, the theory correctly validates that only the portion of the target that the laser beam illuminates can be visualized. The theory provides insights into optimizing photoacoustic SLSC image display based on short-lag value, M, and the illuminating beam profile, $F(z, \mu_a)$.

Future experiments will expand the optical fiber beam profile for complete target illumination and add acoustic scatterers to the target solution. Despite the current absence of acoustic scatterers, the match between theoretical and photoacoustic SLSC data from scatter-free photoacoustic targets of varying sizes is promising, but the absence of scatters likely contributes to the narrow target visualization area. We will additionally fine-tune the theoretical photoacoustic signal profiles to remove oscillations and pursue the development of a simulation package dedicated to coherence-based imaging.

References

[1] M. A. Lediju, G. E. Trahey, B. C. Byram, and J. J. Dhal, "Short-lag spatial coherence of backscattered echose: Imaging characteristics," *IEEE Transactions on Ultrasonics, Ferroelectrics, and Frequency Control*, 2011.

[2] R. Mallart and M. Fink, "The van cittert-zernike theorem in pulse echo measurements," *Acoustical Society of America*, 1991.

[3] P. Beard, "Biomedical photoacoustics," *Interface Focus*, 2011.

[4] M. A. L. Bell, N. Kuo, D. Y. Song, and E. M. Boctor, "Short-lag spatial coherence beamforming of photoacoustic images for enhanced visualization of prostate brachytherapy seeds," *Biomedical Optics Express*, 2013.

[5] M. A. L. Bell, X. Guo, H. J. Kang, and E. M. Boctor, "Improved contrast in laser-diode-based photoacoustic images with short-lag spatial coherence beamforming," *2014 IEEE International Ultrasonics Symposium*, 2014.

[6] M. Xu and L. V. Wang, "Universal back-projection algorithm for photoacoustic computed tomography," *Physical Review*, 2005.